Perspective

Ice Interfaces: Vapor, Liquid, and Solutions

Mary Jane Shultz,* Emma F. Gubbins, Rebecca G. Davies, Zhenyu Lin, and Ziqing Xiong

Read Online

ACCESS | Metrics & More | Article Recommendations

ABSTRACT: Interfaces between hexagonal ice and its vapor, liquid water, and aqueous solutions are all of central importance to life on earth. Despite its importance, much remains unknown about the ice interface, particularly at the molecular level. This contribution contains a brief survey of these three interfaces, emphasizing experimental results. Remarkably, evidence suggests that the secondary prism face is the most stable face at both the ice−vapor and the ice−water interfaces. The ice−aqueous solution interface can be used to generate unique materials. Directional freezing, using a strong thermal gradient, results in kinetic control of ice morphology. Surprisingly, even under these far-from-equilibrium conditions, the secondary prism face is the most stable. A molecular-level justification of this stability is presented.
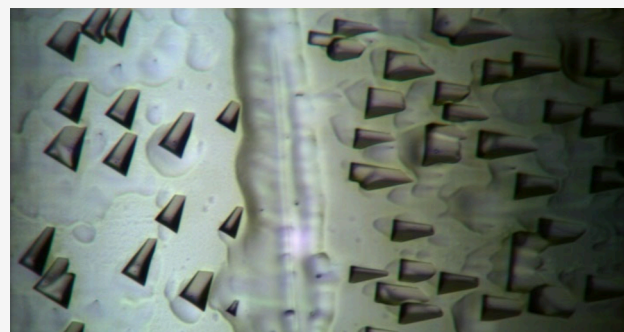
1. INTRODUCTION

Life on earth would not be possible without water. Water mediates interactions among biological molecules, is responsible for weathering, transports materials around the globe, and exchanges species with the larger universe; it literally shapes our world on all scales from the atomic to the cosmic. Despite having only three atoms, water is a complicated material. At last count, there are 19 identified ice phases! A comprehensive review would be extremely long, hence this contribution focuses on the common form of ice at atmospheric pressure: hexagonal ice, I_h (Figure 1). (The fundamental structure of ice is that of a hexagonal prism. This is the first ice structure discovered, so it is labeled I_h denoting first and hexagonal.) More than 400 years ago, before the existence of molecules was known, Kepler[1] pondered the relationship between building

block packing and the hexagonal snowflake shape. We now know that the core of a snowflake consists of a single crystal of hexagonal ice, I_h. The lacy structure of snowflakes builds on this single-crystal core.

A core component of water's central role hinges on its liquid−solid phase transition, a transition that occurs just 10% below ambient temperature, releases significant heat, and is accompanied by a volume expansion. At the molecular level, the source of water's unique place is its extended hydrogen-bonded structure consisting of covalent and H-bonded valences in equal measure. Even in the absence of defects, there is considerable flexibility connected with which of the four hydrogen atoms surrounding the oxygen atom are H-bonded and which are covalently bonded, a flexibility that nets a residual entropy at 0 K.[2] Water's flexible bonding structure presents a challenge both theoretically and experimentally; some of these challenges are highlighted in the discussion.

Not surprisingly, due to the key roles water and ice play, there have been numerous investigations of ice growth, particularly from the vapor phase. The thread that runs through this synopsis builds on Kepler's pondering: the
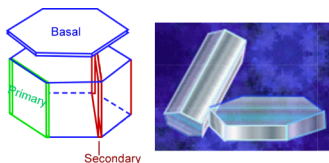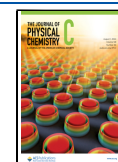

Figure 1. (Left) Hexagonal prism schematic showing the three major faces: (blue) the basal face that imparts a hexagonal shape to snowflakes, (green) the primary prism face (the flat sides of the hexagonal prism), and (red) the secondary prism face, a cut across adjacent apexes. (Right) Growth conditions impact the height:width aspect ratio from needles to flat plates.
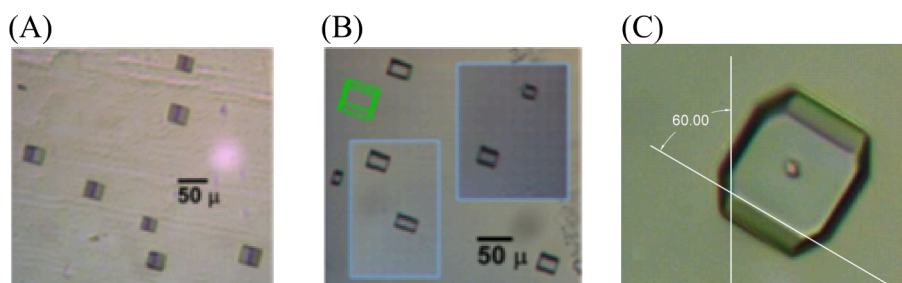
Figure 2. Representative etch pits from (A) the secondary prism $\{11\bar{2}0\}$ and (B) primary prism $\{10\bar{1}0\}$ faces (green outlines show the pit profile). Magnified, large primary prism pits (C) contain pyramidal plane corners. Note that the angle between the *c* axis and the pyramidal face is 60°, indicating a $\{10\bar{1}1\}$ face. Sublimation at −15 °C in an exactly saturated atmosphere. (A and B) Copyright 2015 National Academy of Sciences, ref 119.

molecular-level structure. This contribution begins with a brief overview of ice-vapor results; the major focus is on growth at the ice−liquid interface, with a strong bias toward experimental work. The ice−water interface participates in phenomena including frost heaves, organ preservation, food storage, ice skating, and antifreeze proteins that protect cold climate organisms. Converse to ice prevention, there is also interest in promoting ice formation (e.g., cloud seeding to produce rain, making snow for recreational purposes, and countering the large energy release that accompanies flash freezing when water is supercooled). The third and last sections contain a discussion about exploiting the propensity of ice to exclude solutes present in the liquid to fabricate materials with desired properties. In brief, solutes are swept into grain boundaries as ice forms and hence are concentrated. Since water expands when it freezes, the confined volume is under high pressure. The result is the formation of materials with unique pore and wall structures.

2. ICE−VAPOR INTERFACE

As with many materials, the ice−vapor interface has been investigated under ultrahigh vacuum (UHV) conditions. UHV results lay a foundation for a molecular-level picture.[3,4] Initially, ice deposits on the substrate (usually a metal: Pt, W, or Ag) as amorphous solid water (ASW). As the temperature is raised, ASW converts to crystalline ice.[4] Interestingly, as the ice crystallizes, it dewets the surface with the result that the crystallization temperature depends on the ice film thickness. Dewetting is attributed to the structure of the first monolayer: on metals, first-layer water molecules are fully coordinated, lacking both dangling −OH (*d*-OH) and lone pairs (*d*-O). The normal chair hexagonal shape of ice is flattened due to interactions with the substrate. Additional layers of water thus have no receiving valence for attachment; hence, the surface water layer is hydrophobic and water dewets the surface despite being covered with a monolayer of water, one of the experimental challenges presented by ice. The dewetting phenomena may be relevant to the nucleation of ice in the environment since atmospheric ice typically forms on particulate matter including pollen, dust, soot, and salts that result from ammonia neutralization of acidic gases common in the atmosphere.[5−8] The mismatch between the first solvation layer and ice likely impacts both growth kinetics and the fate of the nascent nuclei. Interestingly, a graphene overlayer appears to create a template for crystallization due to the planar structure of graphene preventing wrinkle defects;[9] crystallization then propagates layer-by-layer in a linear fashion. Relevant to atmospheric conditions, observing layer-by-layer

growth in UHV requires capping of the film to prevent ice formation at the ASW−vacuum interface. An outer surface ice layer propagates from the vacuum toward the template, trapping ASW and altering growth kinetics. Referring again to the atmosphere, ice particles are commonly covered with an adsorbate layer, perhaps protecting the seed from freezing in an out-to-in configuration. Since water expands on freezing, any outer frozen layer would act like a tempering layer, putting strain on the interior and altering the morphology of the resulting ice.

Probing ice−vapor growth near freezing temperature under ambient as opposed to UHV, low-temperature conditions is challenged both by a premelted surface layer and the mechanical softness of the ice surface. For example, atomic force microscopy, used to successfully produce atomic-resolution images of many surfaces, is plagued by a water column that forms a bridge between the surface and the tip. Optical methods are not so plagued; one method that has been successfully applied is laser confocal, differential interference microscopy (LC-DIFM).[10−13] LC-DIFM enables height difference resolution at the surface. Briefly, orthogonally polarized and slightly offset beams reflect from the surface; after polarization rotation−recombination, interference between these two beams revels height differences on the subnanometer scale. LC-DIFM has shown that ice grows in a surface film by spiral growth with a step-edge height of one bilayer.[14] However, the ice surface is not homogeneous, exhibiting both droplets and films on the basal face.[15] The source of this spiral growth was revealed by STM.[16−18] Inevitable step edges in the substrate are nearly the same height as half of the ice *c*-axis lattice constant. Growing films of hexagonal ice that meet at such a boundary cannot smoothly cross the boundary, so the boundary is bridged with cubic ice, creating a grain boundary. Ultimately, the step edge heals, creating a twist in the overlying film where cubic ice bridging the step dislocation meets hexagonal ice.

The inverse of ice growth is ice sublimation. One method to visualize face-specific sublimation is by etching: coat the surface with a thin polymer film,[19−21] and pinholes in the film allow water to sublimate, leaving behind a negative impression of a partially submerged, hexagonal-prism ice crystal. Representative structures are shown in Figure 2. Etches reveal information about relative surface energies as follows. The optic axis is along the long dimension of the pit. The pit is capped by basal faces on each end. The length is the selected prism face. Figure 2, panel A constitutes a secondary prism face with basal face end-caps; panel B a primary prism face with basal face end-caps. The consistent orientation of the optic axis
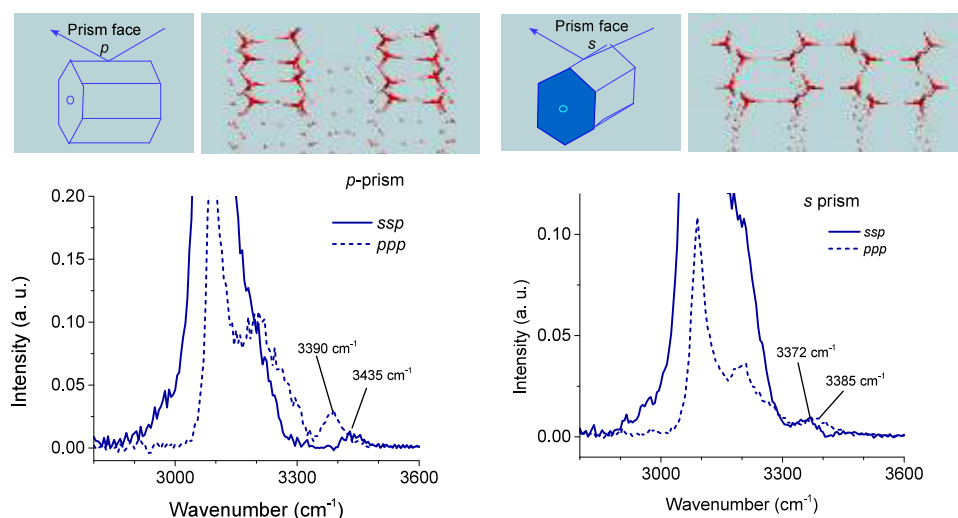
Figure 3. (Top) Schematic of orienting the secondary prism face of ice: cartoon and ball-and-stick model. (Left) *c* axis in the probe plane and (right) *c* axis perpendicular to the plane. (Bottom)[49] SFG spectrum at 110 K with *ppp* and *ssp* polarization for a (left) *p*-oriented surface and (right) *s*-oriented surface. Lower panels adopted from ref 49.

is a testament to the single-crystal nature of the samples. Note that etch pits have consistent profiles over the entire face; the size is dependent on the etch time. With the exception of occasional defects such as glide planes that pin one end forming a truncated pit, face energies are revealed by the height:width aspect ratio using principles of a Wulff construction.[22−25] The ratio reveals the stability of the two prism faces relative to the basal face and thus to each other. The long profile of secondary prism face pits indicates that the secondary face is the most stable. The squarer shape of primary prism pits indicates that this face is only slightly more stable than the basal face. Finally, large primary prism face pits (panel C) exhibit corners between the primary face and the basal endcap; the 60° angle indicates that these corners are {10$\bar{1}$1} pyramidal faces, which are facets that are also observed in STM images of vapor-grown ice.[26] Pyramidal faces are the smallest-area faces and hence the highest energy among the faces shown. Analyzing many pits indicates an energy relative to the secondary prism face of 1.3, 1.8, and 1.9 for the primary prism, basal, and pyramidal faces, respectively.

One method showing great promise for probing ice at the molecular level under atmospheric conditions is nonlinear spectroscopy, sum frequency generation (SFG). Only essential aspects of SFG are described here since several reviews of this technique are available;[27−38] for a comparison of SFG specifically applied to ice and controversies associated with differences, see reference 39. SFG consists of overlapping a visible and an infrared pulse on a surface. The two beams combine only where macroscopic inversion symmetry is broken; all interfaces break inversion symmetry and hence can be probed with SFG provided that the surface is accessible to both the infrared and visible beams. The challenge lies in interpreting the spectrum: the SFG response is complex (in a mathematical sense). The response intensity, *I*, is proportional to the square of the complex polarization, *P*:

$$I \propto |\mathcal{P}|^2 \tag{1}$$

To second order, the polarization is linear in the amplitude of the resonances

$$\tilde{\mathcal{P}}^{(2)} = [\chi_{NR}^{(2)} + \chi_{Res}^{(2)}] : \tilde{E}_{vis}\tilde{E}_{IR} \tag{2}$$

where $\chi_{NR}^{(2)}$ ($\chi_{Res}^{(2)}$) is the nonresonant (resonant) response and $\tilde{E}_{vis}$ ($\tilde{E}_{IR}$) is the visible (infrared) field. (The first-order polarization nets linear IR and Raman responses, and neither is surface-specific.) The resonant part contains information about the vibrational resonances

$$\chi_{Res}^{(2)} = \sum_q \frac{\langle \mu_q \alpha_q \rangle}{\omega_{IR} - \omega_q - i\Gamma_q} \tag{3}$$

where μ_q (α_q) is the dipole (Raman) transition moment, $\langle . . .\rangle$ indicates the spatial average, $\omega_{q(IR)}$ is the resonant (infrared) frequency, and Γ_q is the bandwidth (proportional to $1/\tau$, where τ is the lifetime). If there is a vibrational band, the sum in equation 3 is replaced by an integral over the density of states. The spatial average reveals the source of the surface specificity. Most bulk phases are isotropic on a wavelength scale; the surface is asymmetric, netting a nonzero average. SFG thus probes the surface to the depth at which the asymmetry persists.

The sum then square produces interferences among nearby resonances, resulting both in apparent frequency shifts and in masking weak resonances or those due to minor species at the interface. The solution to this nonlinear challenge is to measure the complex spectral response, hereafter termed complex SFG. As is well known in optics, measuring a complex response requires an interference technique and a phase standard. There have been several techniques to produce the required interference; the currently most used technique is to produce an SFG response from a reference material, generally referred to as the local oscillator, LO, and then interfere the LO signal with that of an unknown sample. This scheme, referred to as heterodyne SFG, has been implemented using both picosecond, *psec*,[40,41] and femtosecond, *fsec*, pulses.[42−44]

Like nearly everything about ice, marrying ice with heterodyne SFG intertwines two challenging areas. The core SFG issue is that the heterodyne technique requires the absence of optics between the LO and the sample—optics introduce phase shifts. Nonetheless, with a creative setup Yamaguchi et al.[45] probed isotopic mixtures of H_2O and D_2O at low temperature (100 K), demonstrating long-range coupling among water molecules leading to a red shift and

narrowing of the resonance with increasing H content. Furthermore, the imaginary (Im) part indicates a net −OH pointing out of the surface, suggesting that the resonance is due to intrabilayer stitching bonds. These have a net dipole pointing out due to the asymmetric environment at the surface.[46,47] Long-range interaction aligns the dipoles, extending the lifetime, netting a narrowed resonance that becomes increasingly narrow as the temperature is lowered.

Ice not only presents challenges but also presents opportunities. Ice is a birefringent material. The prism faces can thus be probed either with the optical c axis in the plane of the two SFG probe beams or with the c axis perpendicular to the probe plane. Here, optical notation is adapted to refer to the former as p orientation and the latter as s orientation. SFG also presents the ability to use polarization to orient the probe beam electric vector. In SFG, there are three beams: the produced sum frequency, the visible excitation, and the infrared excitation. SFG spectra are then labeled with these three polarizations in order: highest to lowest frequency. The most common combination is ssp: s-polarized sum frequency, s-polarized visible, and p-polarized infrared. Ice is a rare exception in that it has both a strong ssp and a strong ppp spectrum (Figure 3).[48] Resonances in the intermediate H-bonded region around 3400 cm^{-1} are reasonably isolated, showing little of the interference normally observed in an intensity or scalar spectrum. The region red of 3300 cm^{-1} is much more intense than that at shorter wavelengths, suggesting that the 3400 cm^{-1} region originates at the surface.

The secondary prism face presents (Figure 3) not only isolated shorter-wavelength peaks but also peaks that depend on both sample- and beam-polarization orientation. These dependences (Table 1) suggest peak assignments.[48] Note that

Table 1. Summary of Secondary Prism Face Modes

Mode (cm^{-1})	Probe polarization	Orientation	Mode type
3372	ssp	s ($\perp c$)	transverse
3385	ppp	s ($\perp c$)	longitudinal
3390	ppp	p ($\parallel c$)	longitudinal
3435	ssp	p ($\parallel c$)	transverse

these are the first dangling valence assignments aside from that of free OH at ∼3700 cm^{-1}. Due to the weaker H-bonds (smaller shift from the free OH), the four observed 3400 cm^{-1} region resonances are expected to be associated with water molecules containing a d-O motif. The two donor hydrogen atoms of such molecules can both be in the plane of the chain, the surface plane; due to canceling in-plane orientations, these are SFG-silent. The four resonances must therefore be due to donor bonds that stitch the top layer to the next. In the secondary prism face, each oxygen atom has only one donor-to-the-next-layer bond. The four resonances can be identified by considering the OH−H configuration of the nearest neighbors in the chain. To bond to the resonating O−H molecule, each nearest neighbor contains one donor and one acceptor within the chain, a dangling valence, and either a donor or acceptor to the next layer. Within the ice rules, the allowed nearest-neighbor configurations (in-chain, cross-chain) are (Figure 4) (i) d-O, d-O; (ii) d-OH, d-O; (iii) d-O, d-OH; and (iv) d-OH, d-OH. (i) Strong longitudinal polarization is created if both nearest-neighbor water molecules adopt a d-O configuration. The two resonances at 3385 and 3390 cm^{-1} are thus assigned to the d-O, d-O, d-O motif with the cross-chain
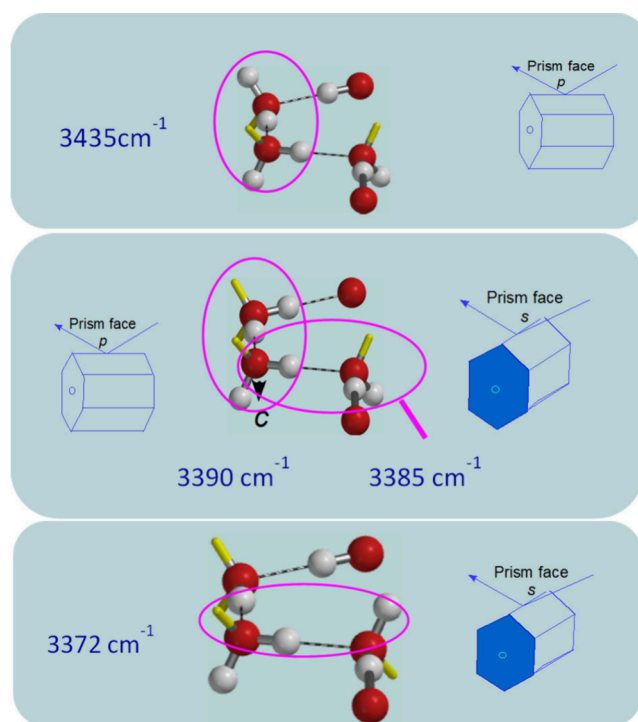

Figure 4. Cartoon showing bilayer stitching motifs from weakest to strongest along with a schematic of the ice hexagonal prism orientation for resonances in the secondary prism face.

coupling slightly stronger than the along-chain coupling (Figure 4, middle panel). Note that the short-wavelength region on the basal face only has a longitudinal mode; it is observed at 3388 cm^{-1}, which is consistent with this assignment.

Nearest neighbors with a d-OH configuration (ii−iv) present a richer response. The dangling −OH disrupts the longitudinal polarization, resulting in transverse polarization. The d-OH neighbor can either be in the chain parallel to the c axis (a p-orientation (ii)) or perpendicular to the c axis (an s orientation (iii)). The p orientation is thus assigned to the weakest stitching resonance (Figure 4 top panel), observed at 3435 cm^{-1}. The s orientation is assigned to the strongest stitching resonance (Figure 4 bottom panel), observed at 3372 cm^{-1}. Finally, if both the parallel to the c axis and the perpendicular to the c axis neighbors have a d-OH configuration (iv), then the polarization is weak; resonance is expected at the average between (ii) and (iii), thus overlapping the longitudinal modes, and is swamped by them.

3. ICE−WATER INTERFACE

Measuring growth at the ice−water interface at the molecular level is considerably more challenging than that at the ice−vapor interface. Scanning techniques do not function well under water, and SFG is unsuccessful since the infrared cannot reach the interface through either the water or the ice. Yet developing a picture of growth at the ice−water interface is important for developing both inhibitors and promoters. Inhibitors enable organisms such as arctic fish and spruce budworm to survive in subzero temperatures, protect organs during cryopreservation, and lead to fun items such as ice cream. On the flip side, seeding clouds with ice promotors provides raindrop nuclei, resulting in rainfall. Seeding is central to forming artificial snow. The current understanding of
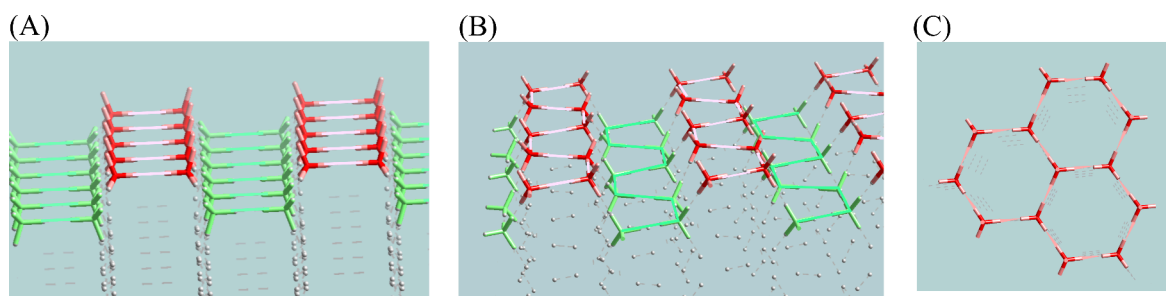
Figure 5. Molecular cartoon of the major faces of ice. (A) The primary prism plane has a bilayer structure. The top half-bilayer consists of water molecule dimers with the water−water bond oriented parallel to the optical, c, axis. (B) The secondary prism face lacks a bilayer structure. The topmost layer consists of chains of H-bonded water molecules; the chain axis is parallel to the c axis. (C) The basal face has a bilayer, hexagonal shape. Note that the six points of a snowflake coincide with the hexagon formed by connecting the top half-bilayer dangling valences. The more open structure of the basal face results in a lower density of d-OH bonds there.

growth at the ice−water interface stems from three areas: (1) splat assays of crystal size, morphology and number from solution, (2) solidification of droplets placed on single-crystal surfaces, and (3) equilibrium growth observations. Each of these is described below.

The splat assay technique originated in 1988[50] as a method to characterize proteins that protect their host from damage under freezing conditions.[51] This damage results in part from the 10% expansion as liquid water becomes ice; the larger volume of ice causes cells to burst. One model for protection is to generate a critical concentration of protein in the extracellular fluid that both induces the formation of nanoscopic ice crystallites[52] and inhibits the growth of larger crystals.[53,54] Within this picture, the protein has both an ice-face templating region and typically a more hydrophobic region.[55−57] The splat assay builds on this idea, measuring inhibition by dropping water droplets onto a cold substrate (typically about −80 °C), thereby generating a large number of small crystallites due to flash freezing the sample, warming the resulting polycrystalline sample to a subzero temperature (−8 °C is typical), and holding the sample at this annealing temperature for a prescribed period. Consistent with a model of limiting ice crystallite size, splat assay analysis consists of either counting the number of crystals or measuring the morphology of the surviving crystals.[58] Linking the splat assay with mutagenesis and fluorescent tagging[57] identifies parts of the protein that are essential for ice recrystallization inhibition (IRI). The result is a picture of the protein containing both ice-templating and hydrophobic regions. Within this broad stroke description, there are several open questions: Does the protein actually bind to the nascent ice crystal, or is it separated from the crystal by one or more quasi-liquid layers of water? Does the attached or solvent-separated protein create a curved indentation in the crystal face that inhibits overgrowth due to the Kelvin effect?[59,60] Molecular-level data could aid in answering these questions.

The splat assay is typically used with a buffer and a high salt content:[61] 10 mM, pH 7.4 phosphate buffer, [NaCl] = 0.138 M, and [KCl] = 0.0027 M. Both pH and high salt are known to modify the structure of water at the air−water interface,[62−65] where anions and cations have different concentration gradients from the gas phase to the bulk concentration. This differential distribution of anions and cations creates an electric double layer, first suggested by experimental results[64,66] and later supported by MD simulations.[67] This picture changes only slightly at the ice−water interface where theoretical models also find a double layer[68] due to the propensity for ice

to exclude solutes. Frozen salt-water ice incorporates ions mainly at pockets or in the grain boundaries,[69,70] a property that is exploited in freeze-desalination. Double layers are well known in electrochemistry, profoundly altering the distribution of ions and the orientation of larger molecules in the interfacial region. Thus, it is expected that the structure of proteins as well as that of the water is altered at the salt-buffer aqueous−ice interface. Further studies are needed to determine if the protein floats on a liquid-like layer or is directly attached and how the buffer and salt concentrations impact the structure. If the protein floats, then detaching ice from a protein-covered surface is expected to be more facile than if ice directly attaches to such a surface.

The molecular-level picture suggested by splat assays motivates the investigation of growth at specific ice faces. One approach is to generate a single crystal with a selected face exposed, put a drop of water on the face, and examine the crystal structure of the resulting frozen droplet. Since ice should form a perfect template for itself, single-crystal growth is expected. As with many aspects of ice, that is not what is observed.[71] Instead, while droplets on the prism face have the same orientation as the underlying crystal (the single crystal templates a single crystal) on the basal face, many crystallites are formed (the single crystal does not net a single crystal in the frozen droplet). The crystallite c axes are tilted randomly along one of the three a axes of the hexagonal substrate. Since the search for ice nucleating materials is often based on the notion that the substrate should template the ice structure,[72] lack of registry on the basal face is curious. A possible explanation for this phenomenon lies in the molecular-level structure of the secondary prism plane—the growth direction with the a-axis tilt observed. As illustrated in Figure 5, both prism faces have a greater density of dangling valences than does the basal face. This tighter structure could result in anisotropic thermal conductivity and thermal gradients within the liquid layer.[71] Alternately, stacking disorder due to inevitable screw dislocations on the basal face as nuclei seeded at different locations meet might be the source of the multiple crystallites. As growing crystallites collide out of registry, growth is favored in the a direction due to its nonbilayer structure. Since the secondary prism face lacks a bilayer structure, it templates single-crystal growth without interference. In a similar manner, the primary prism face, though it has a bilayer structure, lacks a 90° stacking fault layer-to-layer matchup. Consequently, stacking faults favor continued growth with a secondary face exposed. Further experimental and theoretical work is needed to resolve these alternatives.

The relative stability of the basal, primary, and secondary prism faces is also shown by equilibrium growth at the ice–water interface.[73] The challenge in growing ice under equilibrium conditions (0 °C, 1 atm) is overcoming water's tendency to supercool.[74−81] If water is supercooled, ice grows under kinetic control, netting dendritic structures. Avoiding supercooling requires a seed. There are several methods to provide the seed. (1) A single ice crystal formed on the cold enclosure falls and lands on the chilled water surface. Molecular density and hence mass density are lower along the *c* axis, so the seed orients with the *c* axis perpendicular to the surface, thus seeding a single crystal with the *c* axis along the growth direction.[82−84] Long crystals tend to rotate the *c* axis perpendicular to the growth direction as does lake ice.[85] (2) A Czochralski method[86−88] in which a single crystal is solvent glued to a coldfinger, lowered into prechilled water and slowly withdrawn. Success is seed-orientation-dependent. (3) A modified Bridgman−Stockbarger[73,89,90] (B−S) method. The latter two generate greater reproducibility and reliability than the former.

All methods overcome supercooling: methods (1) and (2) use a single crystal to seed growth. While effective, these methods give little information about growth at the ice−water interface due to seed biasing growth. In contrast, the B−S method avoids supercooling by supplying a polycrystalline seed due to flash freezing water in the bulb (Figure 6). Presenting a
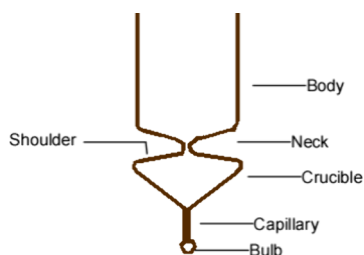

Figure 6. Schematic of a modified Bridgeman−Stockbarger apparatus for single-crystal ice growth. Supercooling is avoided by flash freezing water in the bulb. The tube is lowered from a region slightly above 0 °C through an annulus to a region slightly below. The polycrystalline seed in the bulb evolves through the capillary to the crucible. Typically, fewer than 4 domains enter the crucible. Only one domain intersects with the neck, and the remainder terminate on the shoulders. One domain seeds the remainder of the tube, netting a single crystal that is 2.5 cm in diameter and up to 10 cm long, limited only by the drive screw of the lowering stepper motor and the crucible length.

plethora of faces for seed growth, growth data are garnered via competitive evolution through the lower part of the growth tube. As the tube is slowly (0.1 μm·s^{-1}) lowered through a zero-degree zone, the various ice−water interfaces compete with the more stable faces excluding less-stable ones. Upon emerging from the ∼4 mm capillary, typically fewer than 4 domains remain (often only one). These few domains propagate through the crucible where usually only one (95% yield) intersects the neck and seeds the remaining growth tube. The growth tube thus contains a frozen record of the most stable face. The key question is how the ice single crystal is oriented with respect to the boule axis. Growth is classified as follows. It is basal-growth if the *c* axis is tilted less than 45° with respect to the boule. Prism face categorization is based on the hexagonal cross section: *a* axes are separated by 120°, so the hexagon is subdivided into 6 sections (60°). The 60°

section is further subdivided into primary and secondary prism faces. The prism faces are thus categorized according to the angle between the nearest *a* axis and the boule-growth axis: as a secondary prism face for angles between −15 and +15° and as a primary prism face for angles between +15 and +45° (15−30° is redundant with 45−30°). A representative scatter plot using this classification is shown in Figure 7A. (Results in Figure 7B are discussed below.)

Note that basal face growth is never observed over hundreds of boules, an observation consistent with the drop solidification experiment described above. Lack of basal face growth indicates that the prism faces are more stable than the basal face. Interestingly, both prism faces appear in nearly balanced numbers. Equally interesting, nearly all boules are tilted away from perfect prism face growth. Perfect prism faces would have a tilt angle of 90°; most are tilted between 70 and 80°. Such a tilt is consistent with pyramidal faces observed at the ice−vapor interface.[26]

A simple Gibbs free energy model rationalizes observations at the ice−water interface. Enthalpy is dominated by the endothermic heat of fusion as the fluid water−water bonds are replaced with bonds in ice. Enthalpy is thus determined by the density of the dangling valences: docking onto the dangling valence releases the heat of fusion. Entropy is estimated following Pauling's model of ice:[2] within the ice rules (four valences around each oxygen atom, two and only two covalent bonds to hydrogen), the configurational entropy of bulk ice is S/Nk_B, where k_B is Boltzmann's constant. The surface layer has additional entropy due to the dangling valences lacking an oxygen atom bonding partner, hence the configuration is more flexible. All faces contain one dangling valence per top half-bilayer oxygen atom (or top monolayer if lacking the bilayer structure). The entropy difference among them comes from restrictions on bonding between the vanguard layer and the underlying layer; restrictions are due to simultaneously docking and satisfying the ice rules. Consider the secondary prism face, its vanguard layer consists of H-bonded chains of water molecules that must be properly arrayed to bind onto the underlying layer, thus restricting allowed chain configurations. The primary prism face vanguard layer contains pairs of H-bonded water molecules. The free ends enable many more configurations, hence the greater entropy of the primary prism face. The basal face is the most restricted since the top half-bilayer is connected to the lower half by three bonds; only one valence is free. Configurational entropy and entropy per unit area relative to bulk ice are summarized in Table 2.

Growth at the ice−water interface is of interest in fields ranging from cloud seeding[91,92] to organ preservation[56] to ice prevention on airplanes.[93] As discussed above, experimentally probing growth at the ice−water interface is challenging, a challenge made even greater if the goal is to probe the impact of solution additives to build a molecular model for effective ice-growth modifiers.[52,53,94−96] At the present time, the most common assays are the splat assay and the sucrose sandwich assay.[97] The common thread connecting these two assays is measuring the average crystallite size/number. Along with theoretical models,[98,99] these data net a molecular-level model of interactions among water, ice, and the growth modifier. B−S-grown ice shares common steps with the splat assay and can be used to test splat-assay-based models. Splat assays begin with a polycrystalline seed formed when water droplets impinge on a cold surface, often at −77 °C. Flash freezing water in the growth-crucible bulb freezes the bulb droplet, also
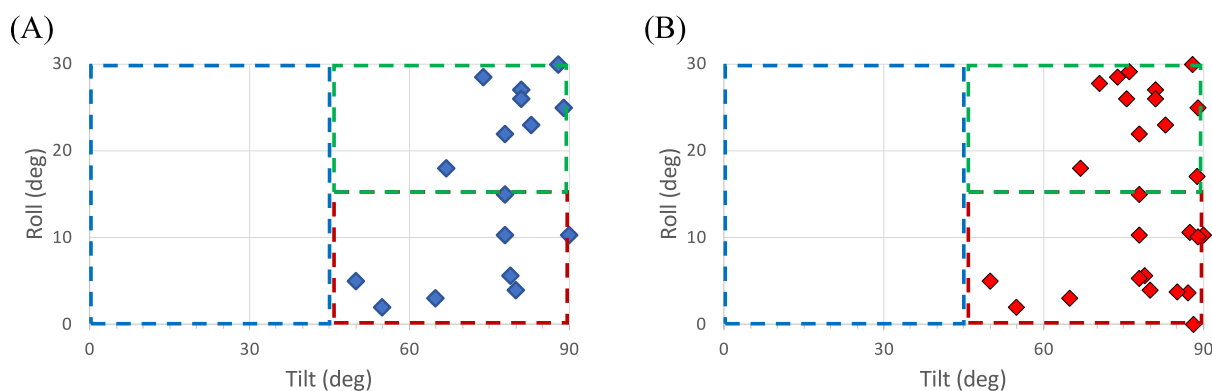
Figure 7. Representative growth data for (A) neat ice−water and (B) ice−PVA solution. Boules are classified according to the angle between the crystal *c* axis and the boule growth axis (the tilt angle) and the angle between the nearest *a* axis and the boule growth axis (the roll angle). Boules in the blue outlined area are broadly labeled as the basal face, those outlined in red are labeled as the secondary prism face boules, and those outlined in green are labeled as primary face boules. Note that basal face growth is never observed.

Table 2. Thermodynamic Parameters for Ice Major Faces

Face	Basal	Primary prism	Secondary prism
Enthalpy ($\mu J \cdot cm^{-2}$)	5.57	5.94	6.90
Configurational entropy relative to bulk ice	$\ln(2/3^{1/2})$	$\ln(2/14^{1/4})$	$\ln(2/2^{1/2})$
Entropy/$Nk_B \times 10^{14}$ (cm^{-2})	6.94	8.07	7.20

at −77 °C. The splat assay then anneals the droplet at a moderate, subzero temperature (−6.4 °C is common), during which time small crystallites either grow by Ostwald ripening or inhibit water monomers or clusters from attaching to the faces of the already formed crystal.[100] The B−S-grown ice evolves its ice−water structure slowly under equilibrium conditions. Faces compete for added molecules or clusters, with more stable faces growing at the expense of less stable ones. Splat assays and B−S-grown ice thus provide somewhat complementary ice-growth information.

Splat assay results identify poly(vinyl alcohol) (PVA) as the most efficient small molecule with ice recrystallization inhibition activity. The model that emerges is one in which PVA binds irreversibly to the primary prism face, reversibly to the secondary prism face, and not at all to the basal face.[60,101−103]

The B−S growth apparatus would seem to provide a method to test the attachment model: if ice binds irreversibly to the primary prism face, then growth statistics should be highly biased against the primary prism face growth. In addition, if the secondary prism face is sufficiently inhibited, then one might observe basal face growth. Furthermore, PVA might be occluded within the boule. The data (Figure 7B) does not support this conclusion: no basal face growth is observed. Any bias away from the primary prism face growth is modest at best. An analysis of the resulting boule to detect PVA incorporated into the ice structure (by melting cross sections and analyzing for PVA) finds no PVA in the boule and thus contradicts incorporation but rather supports a more dynamic attachment−detachment mechanism of interaction. These conclusions are consistent with microfluidic studies[104,105] that find a modest impact on ice-face growth by PVA. Interestingly, safranin, a cationic dye, appears to be quite effective at modifying ice growth. As a charged molecule, safranine has the ability to orient water molecules in both the

first and second solvation shells, supporting a water-layer model.

In summary, it is not clear whether inhibitors function by binding to ice, reorienting water molecules in their solvation shell to configurations unfavorable for ice formation, and thus "float" on water near the ice surface or another mechanism. This field is ripe for subnanometer probing of the ice−water solute interface.

4. USING ICE GROWTH AS A TEMPLATE

Green processing methods are of considerable current interest with more than 1500 articles annually. Since ice is a green chemical, using ice growth to create novel materials is also of intense current interest for the creation of structured materials in the biomedical,[106−108] energy,[109] separations,[110,111] and clean water sectors.[112−114] Using ice growth is called freeze casting; it leverages the propensity of ice to exclude solutes to the ice−water boundary. Briefly, freeze casting typically uses an insulating sleeve capped with a copper plug to create a strong thermal gradient when the plug contacts a cold surface and generates ice nucleation at sites separated by tens of micrometers. Thermal transport takes over, and the fastest-growing facet rapidly dominates the freeze front. Since the ice domains tend to be on the order of 10 to 50 μm, comparable to cell dimensions, there is biomedical interest in creating materials with the potential to template bone and other tissue structures if the solute is biocompatible. For energy applications,[114] the pore structure facilitates ion access to walls of the material while creating a high surface-to-volume ratio netting more rapid charge−discharge cycles. For separations or clean water applications, ice templating creates a material with uniaxial pores, a 10−50 μm pore diameter, and cm length. With micrometer-sized cross sections, water flows through with little Kelvin pressure yet diffusion times to the cell walls are microseconds. For all of these applications, the fundamental question is how does ice grow and create the confined space of the pore? Answering this question is expected to facilitate tailoring of the pore structure for a given application.

Material in the grain boundary is concentrated and under stress due to the volume expansion of water on freezing.[115] Thus, a device can be generated if the concentrated solute condenses to form a solid material; the grain-boundary structure is reflected in the resulting scaffold. In principle,
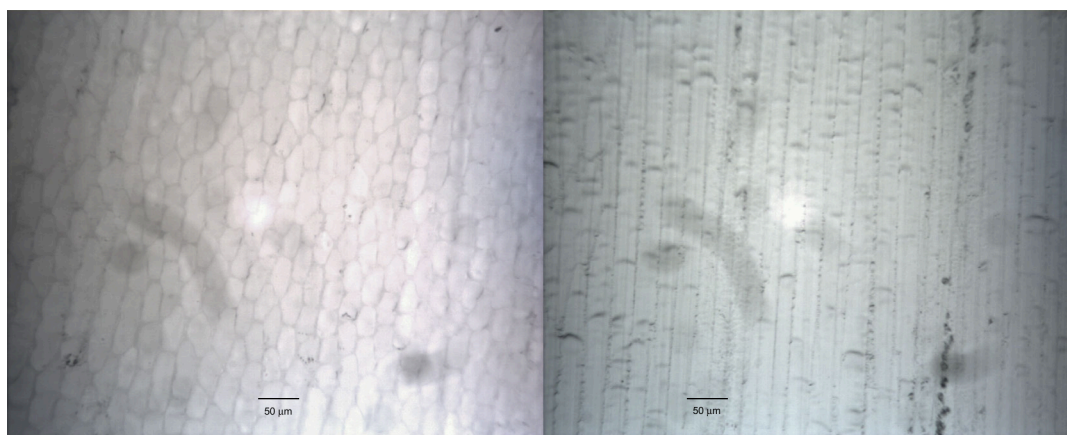
Figure 8. Ice growth characteristics can be used to create materials with unique properties. Solutes are excluded to grain boundaries between growing ice grains, where the solutes can undergo chemical transformation. This process is called freeze casting. Pictomicrograph of a freeze-cast silica scaffold from a 3 M silicic acid solution with a temperature gradient. (Left) Transverse cut showing a honeycomb structure. Note that the long pore dimension varies across the cross section. Pores are ∼40 μm × 10 μm. (Right) The longitudinal cut shows continuously connected channels. Shadows are artifacts from the microscope. Aqueous flow through the structure demonstrates both that the pores are large enough that little head pressure is required for water flow despite the large surface tension of water and that channels are connected, enabling through flow.

the formed scaffold can be recovered simply by letting the ice melt. However, the high surface tension of water (72 mN/m) exerts stress on the nascent scaffold, collapsing the walls, distorting the scaffold, and reducing the mechanical strength. The result is a scaffold that falls apart on handling. One solution to this problem is to exchange water for a lower-surface-tension liquid; a small alcohol is a good choice. The low-surface-tension liquid can be removed by supercritical drying, allowing the scaffold to be heated (supercritical temperature for ethanol is 249−252 °C) without melting, consolidating walls sufficiently to withstand the supercritical drying pressure (5−8 MPa for ethanol).

Remarkably, ice in the pores tends to be single crystal with the a, $\{11\bar{2}0\}$, axis parallel to the temperature gradient:[116] the growth front is the secondary prism face. Herein, it is conjectured that a-axis growth is a result of a confluence of the same smaller exothermicity due to the lower dangling valence density noted in section 3. Released heat counters the strong thermal gradient, so the counterweight is smaller for the secondary than for the other major faces. At the same time, both prism faces have a greater molecular density than the basal face; the stress crushes ice into a-axis growth. The structure of ice is known to respond to applied stress (e.g., forming medium-density amorphous ice when ball milled).[117]

An example of a scaffold formed by this procedure is shown in Figure 8. The cross-sectional structure is remarkably consistent across the entire 5 cm^2 area. In this example, nucleation occurred on a copper plate at 77 K; the sample was contained in a Teflon mold. Teflon is a poor thermal conductor, thus ensuring a reasonably uniform temperature within the cross section. Thus, the traveling freeze front progresses uniformly up the cylindrical mold. The result is that pores do not consolidate, bend, or otherwise distort. The longitudinal cut confirms this picture, with pores extending from the bottom to top of the plug. As shown in Figure 8, there are veins where pores are uniformly oriented, but adjacent veins are rotated on their axes. The result is facile flow along the pore direction. As a bonus, the capillary pore size enables wicking of aqueous solutions into the channels. This opens the potential to coat the walls by using suitable chemical reactions with the dangling −OH groups on the silica surface

to assist with molecular separations or as a platform for chemical reactions.

5. SUMMARY

This contribution is a tour through ice interfaces: ice−vapor, ice−liquid, and ice−solutes. Ice is known to form many crystalline structures. This contribution narrows the focus to hexagonal ice (Figure 1), the stable form under ordinary earth conditions. Although familiar for millennia, much is still unknown about ice growth at interfaces, particularly at the molecular level. The surprising conclusion is that the basal face, the face responsible for the hexagonal shape of snowflakes, is not the most stable of the three major faces at the ice−vapor, ice−water, and ice−aqueous-solution interfaces.

Under equilibrium conditions, slow sublimation under saturated conditions, the most stable face, is the secondary prism face. This conclusion is based on etch pits formed on single-crystal samples and Wulff construction; the largest exposed face is the most stable, and conversely, the smallest is the least stable. Macroscopic boules 2.5 cm diameter and more than 10 cm long cut to expose the primary prism face show rectangular etch pits with parallel shadowed sides (Figure 2). The bottom and sides of these pits comprise primary prism faces, while the end caps are basal faces. Just slightly longer than wide, this suggests that the primary prism face is more stable than the basal face. Similarly, a boule cut to expose the secondary prism face generates pits that are rectangular with a single dark line centered between the long edges. Sublimation occurs along the a axis. Again, the end-caps of the figure are basal faces. The height:width ratio reveals that the secondary prism face is nearly twice as stable as the basal face. Primary prism face etches reveal an additional surprise; as pits grow, they maintain the same shape unless a high-energy face cuts diagonally between faces. Thus, there is a pyramidal face that makes a 60° angle to the basal face—Miller index $\{10\bar{1}1\}$— which is slightly higher in energy than either the basal or the primary prism faces. The energies of the higher-energy faces relative to the most stable secondary prism face are primary prism face = 1.3, basal face = 1.8, and pyramidal face = 1.9.

Probing the ice−water interface under equilibrium conditions is challenged by the tendency of water to supercool to

as low as −46 °C.[78] Supercooled water solidifies rapidly because of kinetic growth. Equilibrium growth requires a seed. Three methods that successfully grow single-crystal ice are (1) soft landing a single crystal on 0 °C water,[82−84] (2) a Czochralski method,[86−88] and (3) a modified Bridgman−Stockbarger[73,89,90] (B−S) method. The former two bias growth due to the seed (1) and by single-crystal seed orientation (2). In contrast, the B−S method starts with the flash freezing of water. A plethora of faces in the polycrystalline seed undergo competitive growth under quasi-equilibrium conditions (slow growth, about 1 bilayer/ms). Ultimately, only one domain seeds a large boule (∼4 cm² cross section and up to 15 cm long). Optical inspection shows that the boule is optically perfect. The boule cross section contains a frozen record of the boule growth. Like the case for tree rings, the cross section can be analyzed to determine growth. Crystal orientation is characterized by a tilt angle, θ (the angle between the c axis and the growth axis) and a roll angle, φ (the angle between the crystal a axis and the growth axis). Growth is classified broadly as basal if the tilt is less than 45° and prism if the tilt is greater than 45°. Nonbasal growth is further subdivided as secondary prism if the roll angle is less than 15° and primary prism if the roll angle is between 15 and 30°. No basal face growth is observed. This indicates that among the three major faces, the basal face has the highest energy at the ice−water interface. Nearly equal primary and secondary face growth indicates a close balance between these two faces. A simple model analogous to Pauling's determination of the residual entropy of ice[118,119] shows that the primary prism face is entropy-favored and the secondary prism face is enthalpy-favored.

Two properties of ice make it a favorable substance for templating materials: (1) ice excludes solutes from its bulk and (2) ice grows with needle-like structures having high length to width ratios. Ice is thus a desirable material for a method called freeze casting.[120−125] Freeze-cast conditions feature high temperature gradients; these are far from equilibrium conditions. Remarkably, it has been found that ice in the pores between grain boundaries is oriented with the a axis parallel to the thermal gradient.[116] The c axis of various grains appears to be randomly oriented around a cone about the growth direction. Armed with this image, the picomicrograph shown in Figure 8A suggests that grains grow with differing c-axis orientations until they collide with neighboring grains. Solutes accumulate in the collision region, where the solute is concentrated under stress. The grain size is highly dependent on the temperature gradient as well as the solute composition. Those shown in Figure 8 are about 40 μm × 10 μm with submicrometer walls. Ice in the pore grows under confinement by the material in the grain boundaries. Water expands when it freezes, tending to push the ice along the thermal gradient. The result is continuous channels for the length of the plug, as shown in Figure 8B. This long, fine capillary structure is ideal for liquid water flow under low head pressure (i.e., laminar flow). The diffusion time from the capillary center to the walls is on the order of microseconds, ideal for ensuring interaction between solutes and materials attached to the walls.

Separating the generated structure from the ice template, in principle, involves simply melting the ice. However, the high surface tension of water causes stress on the walls, collapsing and distorting the newly formed structure. One method to avoid the surface tension problem is to soak the frozen plug in a water-miscible, lower-surface-tension liquid with a freezing point lower than that of water. As the ice melts, water mixes with the replacement liquid. Refreshing the liquid ensures the removal of water. If the chosen liquid also has a relatively low supercritical point, then it can be removed via supercritical drying.[126,127] Ethanol is used in the silica scaffold, as pictured in Figure 8.

The short summary of ice growth is that at the ice−vapor and ice−water equilibrium surfaces as well as at the ice−solute kinetically grown surface, a-axis growth appears to be favored. In contrast, c-axis basal-face growth is disfavored. Kinetic growth along the six hexagonally configured a axes makes the beautiful snowflakes often observed, answering Keppler's question of 400 years ago.

■ AUTHOR INFORMATION

Corresponding Author

Mary Jane Shultz − *Chemistry Department, Tufts University, Medford, Massachusetts 02155, United States;* ● orcid.org/0000-0001-5625-1675; Email: Mary.Shultz@Tufts.edu

Authors

Emma F. Gubbins − *Chemistry Department, Tufts University, Medford, Massachusetts 02155, United States*

Rebecca G. Davies − *Chemistry Department, Tufts University, Medford, Massachusetts 02155, United States;* ● orcid.org/0000-0002-4135-3713

Zhenyu Lin − *Chemistry Department, Tufts University, Medford, Massachusetts 02155, United States*

Ziqing Xiong − *Chemistry Department, Tufts University, Medford, Massachusetts 02155, United States*

Complete contact information is available at:
https://pubs.acs.org/10.1021/acs.jpcc.4c02806

Notes

The authors declare no competing financial interest.

Biographies

Mary Jane Shultz received her B.S. degree in chemistry from the University of Wisconsin, Madison and her Ph.D. degree in theoretical chemistry from M.I.T. After postdoctoral stints at Berkeley and Harvard, she joined the chemistry department at Tufts University. She is a Fellow of the American Academy of Sciences and of the American Chemical Society. Her research interests focus on using fundamental physical chemistry to unravel reactions and interactions, particularly at surfaces, and then leveraging interactions to create practical devices.

Emma F. Gubbins received her B.A. in chemistry from Smith College in 2018 where she studied aerosols under Dr. Andrew Berke. She worked in a trace metals analysis laboratory for one year between undergraduate and graduate school. Emma is currently a Ph.D. candidate at Tufts University working under Dr. Mary Jane Shultz. She is interested in environmental chemistry and spectroscopy. Currently she is studying ice interfaces using sum frequency generation (SFG) spectroscopy.

Rebecca G. Davies completed her chemistry Ph.D. in 2024 from Tufts University, concurrent with an internship in the Office of Technology Transfer and Industry Collaboration. Her graduate work focused on the spectroscopic investigation of catalytic thin films and the development of a scaffold meeting diverse material requirements to support nanoscale photocatalysts. She is currently a postdoctoral scholar at Tufts University developing methods to make phase-sensitive measurements of buried interfaces using sum frequency generation (SFG) spectroscopy. Her interests include optimizing and

commercializing materials and methods for practical applications centered around energy and the environment.

Zhenyu Lin completed a bachelor's degree in chemistry from Hobart and William Smith Colleges and a master's degree in chemistry from Tufts University. Currently, Zhenyu is pursuing a Ph.D. in chemistry at Tufts University and joined the Shultz laboratory in 2021. His research focuses on the study of TiO_2-based nanoparticles and the creation of a support scaffold. His scientific interests include physical chemistry, nanotechnology, and materials science.

Ziqing Xiong completed his undergraduate study and obtained a B.S. degree in chemistry from Peking University, Bejing, China in 2019. He has been a graduate student pursuing his Ph.D. degree in chemistry in the Shultz laboratory, Tufts University, MA since 2020. With a comprehensive interest in chemistry, physics, and math, he expends most of his effort studying physical chemistry. He is currently working on instrument design and nonlinear spectroscopy.

■ REFERENCES

(1) Kepler, J. *On the Six-Cornered Snowflake*; Godfrey Tampach: Frankfort, 1611.

(2) Pauling, L. The structure and entropy of ice and other crystals with some randomness of atomic arrangement. *J. Am. Chem. Soc.* **1935**, *57*, 2680−2684.

(3) Smith, R. S.; Yuan, C.; Petrik, N. G.; Kimmel, G. A.; Kay, B. D. Crystallization growth rates and front propagation in amorphous solid water films. *J. Chem. Phys.* **2019**, *150*, 214703.

(4) Yuan, C.; Smith, R. S.; Kay, B. D. Surface and bulk crystallization of amorphous solid water films: Confirmation of "top-down" crystallization. *Surf. Sci.* **2016**, *652*, 350−354.

(5) Klumpp, K.; Marcolli, C.; Alonso-Hellweg, A.; Dreimol, C. H.; Peter, T. Comparing the ice nucleation properties of the kaolin minerals kaolinite and halloysite. *Atm. Chem. Phys.* **2023**, *23*, 1579−1598.

(6) Stolzenburg, D.; Cai, R. L.; Blichner, S. M.; Kontkanen, J.; Zhou, P. T.; Makkonen, R.; Kerminen, V. M.; Kulmala, M.; Riipinen, I.; Kangasluoma, J. Atmospheric nanoparticle growth. *Rev. Mod. Phys.* **2023**, *95*, 045002.

(7) Prisle, N. L. Surfaces of Atmospheric Droplet Models Probed with Synchrotron XPS on a Liquid Microjet. *Acc. Chem. Res.* **2024**, *57*, 177−187.

(8) Marten, R.; Xiao, M.; Wang, M. Y.; Kong, W. M.; He, X. C.; Stolzenburg, D.; Pfeifer, J.; Marie, G.; Wang, D. S.; Elser, M.; Baccarini, A.; Lee, C. P.; Amorim, A.; Baalbaki, R.; Bell, D. M.; Bertozzi, B.; Caudillo, L.; Dada, L.; Duplissy, J.; Finkenzeller, H.; Heinritzi, M.; Lampimäki, M.; Lehtipalo, K.; Manninen, H. E.; Mentler, B.; Onnela, A.; Petäjä, T.; Philippov, M.; Rörup, B.; Scholz, W.; Shen, J. L.; Tham, Y. J.; Tomé, A.; Wagner, A. C.; Weber, S. K.; Zauner-Wieczorek, M.; Curtius, J.; Kulmala, M.; Volkamer, R.; Worsnop, D. R.; Dommen, J.; Flagan, R. C.; Kirkby, J.; Donahue, N. M.; Lamkaddam, H.; Baltensperger, U.; El Haddad, I. Assessing the importance of nitric acid and ammonia for particle growth in the polluted boundary layer. *Env. Sci.-Atm.* **2024**, *4*, 265−274.

(9) Piao, Z.; Park, J. K.; Patel, M.; Lee, H. J.; Jeong, B. Poly(l-Ala-co-l-Lys) Exhibits Excellent Ice Recrystallization Inhibition Activity. *ACS Macro Lett.* **2021**, *10*, 1436−1442.

(10) Sazaki, G.; Zepeda, S.; Nakatsubo, S.; Yokomine, M.; Furukawa, Y. Quasi-liquid layers on ice crystal surfaces are made up

of two different phases. *Proc. Am. Acad. Arts Sci.* **2012**, *109*, 1052−1055.

(11) Asakawa, H.; Sazaki, G.; Nagashima, K.; Nakatsubo, S.; Furukawa, Y. Two types of quasi-liquid layers on ice crystals are formed kinetically. *Proc. Am. Acad. Arts Sci.* **2016**, *113*, 1749−1753.

(12) Murata, K.-i; Nagashima, K.; Sazaki, G. In situ observations of spiral growth on ice crystal surfaces. *Phys. Rev. Mater.* **2018**, *2*, 093402.

(13) Murata, K.-i; Nagashima, K.; Sazaki, G. How Do Ice Crystals Grow inside Quasiliquid Layers? *Phys. Rev. Lett.* **2019**, *122*, 026102.

(14) Sazaki, G.; Zepeda, S.; Nakatsubo, S.; Yokoyama, E.; Furukawa, Y. Elementary steps at the surface of ice crystals visualized by advanced optical microscopy. *Proc. Nat. Acad. Sci. US* **2010**, *107*, 19702−19707.

(15) Murata, K.-i; Asakawa, H.; Nagashima, K.; Furukawa, Y.; Sazaki, G. Thermodynamic origin of surface melting on ice crystals. *Proc. Nat'l. Acad. Sci. US* **2016**, *113*, E6741−E6748.

(16) Thurmer, K.; Nie, S. Formation of hexagonal and cubic ice during low-temperature growth. *Proc. Nat. Acad. Sci. US* **2013**, *110*, 11757−11762.

(17) Thurmer, K.; Bartelt, N. C. Growth of multilayer ice films and the formation of cubic ice imaged with STM. *Phys. Rev. B* **2008**, *77*, 195425.

(18) Maier, S.; Lechner, B. A. J.; Somorjai, G. A.; Salmeron, M. Growth and Structure of the First Layers of Ice on Ru(0001) and Pt(111). *J. Am. Chem. Soc.* **2016**, *138*, 3145−3151.

(19) Bryant, G. W.; Mason, B. J. Etch pits and dislocations in ice crystals. *Philos. Mag.* **1960**, *5*, 1221−1227.

(20) Barrette, P. D.; Sinha, N. K. Lattice rotation in a deformed ice crystal: A study by chemical etching and replication. *Mater. Chem. Phys.* **1996**, *44*, 251−254.

(21) Higuchi, K. The etching of ice crystals. *Acta Metall.* **1958**, *6*, 636−642.

(22) Wulff, G. On the question of speed of growth and dissolution of crystal surfaces. *Z. Kryst. Mineral.* **1901**, *34*, 449−530.

(23) Saito, Y. Wulff polyhedra Derived from Morse Potentials and Crystal Habits of bcc and fcc Metal Particles. *J. Cryst. Growth* **1981**, *53*, 273−279.

(24) Winterbottom, W. L. Equilibrium Shape of a Small Particle in Contact with a Foreign Substrate. *Acta Metall.* **1967**, *15*, 303−310.

(25) Barnard, A. S.; Zapol, P. A model for the phase stability of arbitrary nanoparticles as a function of size and shape. *J. Chem. Phys.* **2004**, *121*, 4276−4283.

(26) Pfalzgraff, W. C.; Hulscher, R. M.; Neshyba, S. P. Scanning electron miscroscopy and molecular dynamics of surfaces of growing and ablating hexagonal ice crystals. *Atmos. Chem. Phys.* **2010**, *10*, 2927−2935.

(27) Yamaguchi, S.; Otosu, T. Progress in phase-sensitive sum frequency generation spectroscopy. *Phys. Chem. Chem. Phys.* **2021**, *23*, 18253−18267.

(28) Nagata, Y.; Hama, T.; Backus, E. H. G.; Mezger, M.; Bonn, D.; Bonn, M.; Sazaki, G. The Surface of Ice under Equilibrium and Nonequilibrium Conditions. *Acc. Chem. Res.* **2019**, *52*, 1006−1015.

(29) Wang, H.-F. Sum frequency generation vibrational spectroscopy (SFG-VS) for complex molecular surfaces and interfaces: Spectral lineshape measurement and analysis plus some controversial issues. *Prog. Surf. Sci.* **2016**, *91*, 155−182.

(30) Roke, S.; Gonella, G.; Johnson, M.; Cremer. Nonlinear Light Scattering and Spectroscopy of Particles and Droplets in Liquids. *Ann. Rev. Phys. Chem.* **2012**, *63*, 353−378.

(31) Shultz, M. J.; Bisson, P.; Groenzin, H.; Li, I. Multiplexed polarization spectroscopy: Measuring surface hyperpolarizability orientation. *J. Chem. Phys.* **2010**, *133*, 054702.

(32) Tian, C. S.; Shen, Y. R. Sum-frequency vibrational spectroscopic studies of water/vapor interfaces. *Chem. Phys. Lett.* **2009**, *470*, 1−6.

(33) Shultz, M. J. Sum Frequency Generation: An Introduction Plus Recent Developments and Current Issues. In *Advances in Multi-Photon*

Processes and Spectroscopy; Lin, S. H., Villaeys, A. A., Fujimura, Y., Eds.; World Scientific: Singapore, 2008; Vol. *18*, pp 133−200.

(34) Shen, Y. R.; Ostroverkhov, V. Sum-Frequency Vibrational Spectroscopy on Water Interfaces: Polar Orientation of Water Molecules at Interfaces. *Chem. Rev.* **2006**, *106*, 1140−1154.

(35) Shultz, M. J.; Schnitzer, C.; Simonelli, D.; Baldelli, S. SFG Spectroscopy of the Aqueous Interface: Ionic and Soluble Molecular Solutions. *Int. Rev. Phys. Chem.* **2000**, *19*, 123−153.

(36) Shen, Y. R. Phase-Sensitive Sum-Frequency Spectroscopy. *Annu. Rev. Phys. Chem.* **2013**, *64*, 129−150.

(37) Shen, Y. R. *Fundamentals of Sum Frequency Spectroscopy*; Cambridge University Press: Cambridge, U.K., 2016.

(38) Shultz, M. J.; Bisson, P.; Wang, J.; Marmolejos, J.; Davies, R. G.; Gubbins, E.; Xiong, Z. High Phase Resolution: Probing Interactions in Complex Interfaces with Sum Frequency Generation. *Biointerphases* **2023**, *18*, 058502.

(39) Yamaguchi, S.; Suzuki, Y.; Nojima, Y.; Otosu, T. Perspective on sum frequency generation spectroscopy of ice surfaces and interfaces. *Chem. Phys.* **2019**, *522*, 199−210.

(40) Ji, N.; Ostroverkhov, V.; Chen, C.-Y.; Shen, Y.-R. Phase-sensitive sum-frequency vibrational spectroscopy and its application to studies of interfacial alkyl chains. *J. Am. Chem. Soc.* **2007**, *129*, 10056−10057.

(41) Nojima, Y.; Yamaguchi, S. Heterodyne-Detected Sum Frequency Generation Spectroscopic Study of Weakly Hydrogen-Bonded Water at Charged Lipid Interfaces, Revisited. *J. Phys. Chem. C* **2021**, *125*, 23483−23489.

(42) Nihonyanagi, S.; Kusaka, R.; Inoue, K.-i.; Adhikari, A.; Yamaguchi, S.; Tahara, T. Accurate determination of complex $\chi(2)$ spectrum of the air/water interface. *J. Chem. Phys.* **2015**, *143*, 124707.

(43) Lukas, M.; Backus, E. H. G.; Bonn, M.; Grechko, M. Passively Stabilized Phase-Resolved Collinear SFG Spectroscopy Using a Displaced Sagnac Interferometer. *J. Phys. Chem. A* **2022**, *126*, 951−956.

(44) Sun, S.; Bisson, P. J.; Bonn, M.; Shultz, M. J.; Backus, E. H. G. Phase-Sensitive Sum-Frequency Measurements Using a Femtosecond Nonlinear Interferometer. *J. Phys. Chem. C* **2019**, *123*, 7266−7270.

(45) Nojima, Y.; Shioya, Y.; Torii, H.; Yamaguchi, S. Hydrogen order at the surface of ice Ih revealed by vibrational spectroscopy. *Chem. Commun.* **2020**, *56*, 4563−4566.

(46) Ishiyama, T.; Takahashi, H.; Morita, A. Origin of Vibrational Spectroscopic Response at Ice Surface. *J. Phys. Chem. Lett.* **2012**, *3*, 3001−3006.

(47) Otsuki, Y.; Sugimoto, T.; Ishiyama, T.; Morita, A.; Watanabe, K.; Matsumoto, Y. Unveiling subsurface hydrogen-bond structure of hexagonal water ice. *Phys. Rev. B* **2017**, *96*, 115405.

(48) Shultz, M. J.; Bisson, P.; Vu, T. H. Molecular Dance: Water's Collective Modes. *Chem. Phys. Lett.* **2013**, *588*, 1−10.

(49) Bisson, P. J.; Shultz, M. J. Hydrogen Bonding in the prism face of ice I_h via Sum Frequency Vibrational Spectroscopy. *J. Phys. Chem. A* **2013**, *117*, 6116−6125.

(50) Knight, Charles A.; Hallett, John; DeVries, A. L. Solute effects on ice recrystallization: An assessment technique. *Cryobiology* **1988**, *25*, 55−60.

(51) Ramløv, H.; Wharton, D. A.; Wilson, P. W. Recrystallization in a Freezing Tolerant Antarctic Nematode, Panagrolaimus davidi, and an Alpine Weta, Hemideina maori(Orthoptera; Stenopelmatidae). *Cryobiology* **1996**, *33*, 607−613.

(52) Cui, S.; Zhang, W.; Shao, X.; Cai, W. Do antifreeze proteins generally possess the potential to promote ice growth? *Phys. Chem. Chem. Phys.* **2022**, *24*, 7901−7908.

(53) Gruneberg, A. K.; Graham, L. A.; Eves, R.; Agrawal, P.; Oleschuk, R. D.; Davies, P. L. Ice recrystallization inhibition activity varies with ice-binding protein type and does not correlate with thermal hysteresis. *Cryobiology* **2021**, *99*, 28−39.

(54) Tas, R. P.; Hendrix, M. M. R. M.; Voets, I. K. Nanoscopy of single antifreeze proteins reveals that reversible ice binding is sufficient for ice recrystallization inhibition but not thermal hysteresis. *Proc. Nat. Acad. Sci. US* **2023**, *120*, e2212456120.

(55) Ampaw, A. A.; Sibthorpe, A.; Ben, R. N. Use of Ice Recrystallization Inhibition Assays to Screen for Compounds That Inhibit Ice Recrystallization. In *Metolds in Molecular Biology*; Springer, 2021; Vol. *2180*, pp 271−283.

(56) Ampaw, A.; Charlton, T. A.; Briard, J. G.; Ben, R. N. Designing the next generation of cryoprotectants - From proteins to small molecules. *Peptide Sci.* **2019**, *111*, e24086.

(57) Garnham, C. P.; Natarajan, A.; Middleton, A. J.; Kuiper, M. J.; Braslavsky, I.; Davies, P. L. Compound Ice-Binding Site of an Antifreeze Protein Revealed by Mutagenesis and Fluorescent Tagging. *Biochem.* **2010**, *49*, 9063−9071.

(58) Saad, J.; Fomich, M.; Dia, V. P.; Wang, T. A novel automated protocol for ice crystal segmentation analysis using Cellpose and Fiji. *Cryobiology* **2023**, *111*, 1−8.

(59) Nutt, D. R.; Smith, J. C. Dual Function of the Hydration Layer around an Antifreeze Protein Revealed by Atomistic Molecular Dynamics Simulations. *J. Am. Chem. Soc.* **2008**, *130*, 13066−13073.

(60) Bachtiger, F.; Congdon, T. R.; Stubbs, C.; Gibson, M. I.; Sosso, G. C. The atomistic details of the ice recrystallisation inhibition activity of PVA. *Nature Comm.* **2021**, *12*, 1323.

(61) Stubbs, C.; Wilkins, L. E.; Fayter, A. E. R; Walker, M.; Gibson, M. I. Multivalent Presentation of Ice Recrystallization Inhibiting Polymers on Nanoparticles Retains Activity. *Langmuir* **2019**, *35*, 7347−7353.

(62) Mancinelli, R.; Botti, A.; Bruni, F.; Ricci, M. A.; Soper, A. K. Hydration of sodium, potassium, and chloride ions in solution and the concept of structure maker/breaker,. *J. Phys. Chem. B* **2007**, *111*, 13570−13577.

(63) Zhang, Y.-H.; Chan, C. K. Observations of water monomers in supersaturated NaCIO4, LiCIO4, and Mg(CIO4)2 droplets using raman spectroscopy. *J. Phys. Chem. A* **2003**, *107*, 5956−5962.

(64) Schnitzer, C.; Baldelli, S.; Shultz, M. J. Sum Frequency Generation of Water on NaCl, NaNO₃, KHSO₄, HCl, HNO₃, and H₂SO₄ Aqueous Solutions. *J. Phys. Chem. B* **2000**, *104*, 585−590.

(65) Casillas-Ituarte, N. N.; Chen, X.; Castada, H.; Allen, H. C. Na+ and Ca²⁺ Effect on the Hydration and Orientation of the Phosphate Group of DPPC at Air-Water and Air-Hydrated Silica Interfaces. *J. Phys. Chem. B* **2010**, *114*, 9485−9495.

(66) Baldelli, S.; Schnitzer, C.; Jane Shultz, M.; Campbell, D.J. Sum Frequency Generation Investigation of Water at the Surface of H₂O/H₂SO₄ and H₂O/Cs₂SO₄ Binary Systems. *Chem. Phys. Lett.* **1998**, *287*, 143−147.

(67) Jungwirth, P.; Tobias, D. J. Molecular Structure of Salt Solutions: A New View of the Interface with Implications for Heterogeneous Atmospheric Chemistry. *J. Phys. Chem. B* **2001**, *105*, 10468−10472.

(68) Daigle, H. Structure of the electrical double layer at the ice-water interface. *J. Chem. Phys.* **2021**, *154*, 214703.

(69) Luo, S.; Jin, Y. K.; Tao, R.; Li, H. Y.; Li, C.; Wang, J.; Li, Z. G. Molecular understanding of ion rejection in the freezing of aqueous solutions. *Phys. Chem. Chem. Phys.* **2021**, *23*, 13292−13299.

(70) Rasmussen, A.; Jannat, M.; Wang, H. L. Fundamentals of freeze desalination: Critical review of ion inclusion and rejection studies from molecular dynamics perspective. *Desalination* **2024**, *573*, 117216.

(71) Mizuno, Y.; Wakahama, G. Structure and orientation of frozen droplets on ice surfaces. *J. Phys. Chem.* **1983**, *87*, 4161−4167.

(72) Soni, A.; Patey, G. N. Ice Nucleation by the Primary Prism Face of Silver Iodide. *J. Phys. Chem. C* **2022**, *126*, 6716−6723.

(73) Bisson, P.; Groenzin, H.; Barnett, I. L.; Shultz, M. J. High Yield, Single Crystal Ice via the Bridgman Method. *Rev. Sci. Instrum.* **2016**, *87*, 034103.

(74) Guo, Q.; Cheng, P. Effects of non-uniform temperature of the ice nucleus on heterogeneous ice nucleation. *Int. J. Heat Mass Transfer* **2020**, *163*, 120404.

(75) Naullage, P. M.; Qiu, Y.; Molinero, V. What Controls the Limit of Supercooling and Superheating of Pinned Ice Surfaces? *J. Phys. Chem. Lett.* **2018**, *9*, 1712−1720.

(76) Espinosa, J. R.; Vega, C.; Sanz, E. Homogeneous Ice Nucleation Rate in Water Droplets. *J. Phys. Chem. C* **2018**, *122*, 22892–22896.

(77) Gallo, P.; Stanley, H. E. Supercooled water reveals its secrets. *Science* **2017**, *358*, 1543–1544.

(78) Sellberg, J. A.; Huang, C.; McQueen, T. A.; Loh, N. D.; Laksmono, H.; Schlesinger, D.; Sierra, R. G.; Nordlund, D.; Hampton, C. Y.; Starodub, D.; et al. Ultrafast X-ray probing of water structure below the homogeneous ice nucleation temperature. *Nature* **2014**, *510*, 381–384.

(79) Adachi, S.; Yoshizaki, I.; Ishikawa, T.; Yokoyama, E.; Furukawa, Y.; Shimaoka, T. Stable growth mechanisms of ice disk crystals in heavy water. *Phys. Rev. E* **2011**, *84*, 051605.

(80) Libbrecht, K. G. Toward a Comprehensive Model of Snow Crystal Growth: 3. The Correspondence Between Ice Growth from Water Vapor and Ice Growth from Liquid Water **2014**, arXiv:1407.0740.

(81) Nistor, R. A.; Markland, T. E.; Berne, B. J. Interface-Limited Growth of Heterogeneously Nucleated Ice in Supercooled Water. *J. Phys. Chem. B Lett.* **2014**, *118*, 752–760.

(82) Knight, C. A. A simple technique for growing large, optically "perfect" ice crystals. *J. Glaciology* **1996**, *42*, 585–587.

(83) Maruyama, M.; Ashida, T.; A. Knight, C. Disk crystals of ice grown in air-free water: no effect of dissolved air on the morphology. *J. Cryst. Gr.* **1999**, *205*, 391–394.

(84) Knight, C. Structural Approach to Ice Growth (and Nucleation) in Liquid Water. *Cryst. Growth Des.* **2020**, *20*, 580–589.

(85) Petrenko, V. F.; Witworth, R. *Physics of Ice*; Oxford University Press: Oxford, UK, 1999; pp 314–318.

(86) Czochralski, J. Ein neues Verfahren zur Messung der Kristallisationsgeschwindigkeit der Metalle. *Z. Phys. Chem.* **1918**, *92*, 219–221.

(87) Higashi, A.; Oguro, M.; Fukuda, A. Growth of ice single crystals from the melt, with special reference to dislocation structure. *J. Cryst. Growth* **1968**, *3–4*, 728–732.

(88) Higashi, A. Growth and perfection of ice crystals. *J. Cryst. Growth* **1974**, *24–25*, 102–107.

(89) Bridgman, P. W. Certain Physical Properties of Single Crystals of Tungsten, Antimony, Bismuth, Tellurium, Cadmium, Zinc, and Tin. *Proc. Am. Acad. Arts Sci.* **1925**, *60*, 305–383.

(90) Stockbarger, D. C. The Production of Large Single Crystals of Lithium Fluoride. *Rev. Sci. Instrum.* **1936**, *7*, 133–136.

(91) Pelley, J. Does cloud seeding really work? *Chem. Eng. News* **2016**, *94*, 18–21.

(92) Lohmann, U.; Gasparini, B. A cirrus cloud climate dial? Cirrus cloud seeding may help to reduce climate warming, but large uncertainties remain. *Science* **2017**, *357*, 248.

(93) Kreder, M. J.; Alvarenga, J.; Kim, P.; Aizenberg, J. Design of anti-icing surfaces: smooth, textured or slippery? *Nature Rev. Mater.* **2016**, *1*, 15003.

(94) Yang, W.; Liao, Y.; Shi, Q.; Sun, Z. The Atomistic Understanding of the Ice Recrystallization Inhibition Activity of Antifreeze Glycoproteins. *Crystals* **2023**, *13*, 405.

(95) Schwidetzky, R.; Kunert, A. T.; Bonn, M.; Poschl, U.; Ramløv, H.; DeVries, A. L.; Frohlich-Nowoisky, J.; Meister, K. Inhibition of Bacterial Ice Nucleators Is Not an Intrinsic Property of Antifreeze Proteins. *J. Phys. Chem. B* **2020**, *124*, 4889–4895.

(96) Pal, P.; Chakraborty, S.; Jana, B. Deciphering the Role of the Non-ice-binding Surface in the Antifreeze Activity of Hyperactive Antifreeze Proteins. *J. Phys. Chem. B* **2020**, *124*, 4686–4696.

(97) Ampaw, A. A.; Sibthorpe, A.; Ben, R. N. Use of Ice Recrystallization Inhibition Assays to Screen for Compounds That Inhibit Ice Recrystallization. *Methods Mol. Biol.* **2021**, *2180*, 271–283.

(98) Kamat, K.; Naullage, P. M.; Molinero, V.; Peters, B. Diffusion Attachment Model for Long Helical Antifreeze Proteins to Ice. *Biomacromolecules* **2022**, *23*, 513–519.

(99) Hudait, A.; Moberg, D. R.; Qiu, Y.; Odendahl, N.; Paesani, F.; Molinero, V. Preordering of water is not needed for ice recognition by hyperactive antifreeze proteins. *Proc. Nat. Acad. Sci. US* **2018**, *115*, 8266–8271.

(100) Zhang, X.; He, Y.; Sushko, M. L.; Liu, J.; Luo, L.; De Yoreo, J. J.; Mao, S. X.; Wang, C.; Rosso, K. M. Direction-specific van der Waals attraction between rutile TiO_2 nanocrystals. *Science* **2017**, *356*, 434–437.

(101) Naullage, P. M.; Molinero, V. Slow Propagation of Ice Binding Limits the Ice-Recrystallization Inhibition Efficiency of PVA and Other Flexible Polymers. *J. Am. Chem. Soc.* **2020**, *142*, 4356–4366.

(102) Naullage, P. M.; Lupi, L.; Molinero, V. Molecular Recognition of Ice by Fully Flexible Molecules. *J. Phys. Chem. C* **2017**, *121*, 26949–26957.

(103) Bleszynski, M.; Reil, M.; Kumosa, M. Hydroxyl Group Separation Distances in Anti-Freeze Compounds and Their Effects on Ice Nucleation. *Int. J. Mol. Sci.* **2020**, *21*, 8488.

(104) Drori, R.; Li, C.; Hu, C.; Raiteri, P.; Rohl, A. L.; Ward, M. D.; Kahr, B. A Supramolecular Ice Growth Inhibitor. *J. Am. Chem. Soc.* **2016**, *138*, 13396–13401.

(105) Meister, K.; DeVries, A. L.; Bakker, H. J.; Drori, R. Antifreeze Glycoproteins Bind Irreversibly to Ice. *J. Am. Chem. Soc.* **2018**, *140*, 9365–9368.

(106) Iqbal, M. N.; Robert-Nicoud, G.; Ciurans-Oset, M.; Akhtar, F.; Hedin, N.; Bengtsson, T. Mesoporous Silica Particles Retain Their Structure and Function while Passing through the Gastrointestinal Tracts of Mice and Humans. *ACS Appl. Mater. Interfaces* **2023**, *15*, 9542–9553.

(107) Maleki, H.; Shahbazi, M.-A.; Montes, S.; Hosseini, S. H.; Eskandari, M. R.; Zaunschirm, S.; Verwanger, T.; Mathur, S.; Milow, B.; Krammer, B.; Husing, N.; et al. Mechanically Strong Silica-Silk Fibroin Bioaerogel: A Hybrid Scaffold with Ordered Honeycomb Micromorphology and Multiscale Porosity for Bone Regeneration. *ACS Appl. Mater. Interfaces* **2019**, *11*, 17256–17269.

(108) Choi, Y.; Jeong, J. H.; Kim, J. Mechanically Enhanced Hierarchically Porous Scaffold Composed of Mesoporous Silica for Host Immune Cell Recruitment. *Adv. Healthcare Mater.* **2017**, *6*, 1601160.

(109) Buga, M.-R.; Spinu-Zaulet, A. A.; Ungureanu, C. G.; Mitran, R.-A.; Vasile, E.; Florea, M.; Neatu, F. Carbon-Coated SiO_2 Composites as Promising AnodeMaterial for Li-Ion Batteries. *Molecules* **2021**, *26*, 4531.

(110) Su, X.; Tao, J.; Chen, S.; Xu, P.; Wang, D.; Teng, Z. Uniform hierarchical silica film with perpendicular macroporous channels and accessible ordered mesopores for biomolecule separation. *Chin. Chem. Lett.* **2019**, *30*, 1089–1092.

(111) Poryvaev, A. S.; Gjuzi, E.; Yazikova, A. A.; Polyukhov, D. M.; Albrekht, Y. N.; Efremov, A. A.; Kudriavykh, N. A.; Yanshole, V. V.; Hoffmann, F.; Froba, M.; Fedin, M. V.; et al. Blatter Radical-Decorated Silica as a Prospective Adsorbent for Selective NO Capture from Air. *ACS Appl. Mater. Interface.* **2023**, *15*, 5191–5197.

(112) Li, M.; Zhao, N.; Mao, A.; Wang, M.; Shao, Z.; Gao, W.; Bai, H. Preferential ice growth on grooved surface for crisscross-aligned graphene aerogel with large negative Poisson's ratio. *Nat. Commun.* **2023**, *14*, 7855.

(113) Wegst, U. G. K.; Kamm, P. H.; Yin, K.; Garcia-Moreno, F. Freeze casting. *Nat. Rev. Methods* **2024**, *4*, 28.

(114) Franke-Lang, R.; Bansemer, J.; Fleck, C.; Kowal, J. Enhanced Zinc-Air Batteries through the Fabrication of Structured Zinc Electrodes Using Freeze-Casting. *Adv. Eng. Mater.* **2024**, DOI: 10.1002/adem.202400148.

(115) Gerber, D.; Wilen, L. A.; Poydenot, F.; Dufresne, E. R.; Style, R. W. Stress accumulation by confined ice in a temperature gradient. *Proc. Nat. Acad. Sci. USA* **2022**, *119*, DOI: 10.1073/pnas.2200748119.

(116) Donius, A. E.; Obbard, R. W.; Burger, J. A.; Hunger, P. M.; Baker, I.; Doherty, R. D.; Wegst, U. G.K. Cryogenic EBSD Reveals Structure of Directionally Solidified Ice-Polymer Composite. *Mater. Charact.* **2014**, *93*, 184–190.

(117) Rosu-Finsen, A.; Davies, M. B.; Amon, A.; Wu, H.; Sella, A.; Michaelides, A.; Salzmann, C. G. Medium-density amorphous ice. *Science* **2023**, *379*, 474–478.

(118) Brumberg, A.; Hammonds, K.; Baker, I.; Backus, E. H. G.; Bisson, P. J.; Bonn, M.; Daghlian, C. P.; Mezger, M.; Shultz, M. J.

Single crystal I_h ice surfaces unveil connection between macroscopic and molecular structure. *Proc. Natl. Acad. Sci. U. S. A.* **2017**, *114*, 5349−5354.

(119) Shultz, M. J.; Brumberg, A.; Bisson, P. J.; Shultz, R. Producing Desired Ice Faces. *Proc. Natl. Acad. Sci. U. S. A.* **2015**, *112*, E6096−E6100.

(120) Wu, C. Z.; Chen, Z. Y.; Liu, X.; Shen, T.; Zu, L.; Zhang, L. Customizing the Pore Structure and Properties of Freeze-Cast Porous Titanium by Zirconium Acetate Additive. *Ad. Eng. Mater.* **2020**, *22*, 2000519.

(121) Muto, T.; Harada, M.; Fukuhara, G.; Okada, T. Ice Confinement-Induced Solubilization and Aggregation of Cyanonaph-thol Revealed by Fluorescence Spectroscopy and Lifetime Measure-ments. *J. Phys. Chem. B* **2020**, *124*, 3734−3742.

(122) Park, H.; Cho, H.-H.; Kim, K.; Hong, K.; Kim, J.-H.; Choe, H.; Dunand, D. C. Surface-oxidized, freeze-cast cobalt foams: Microstructure, mechanical properties and electrochemical perform-ance. *Acta Metall.* **2018**, *142*, 213−225.

(123) Scotti, K. L.; Dunand, D. C. Freeze casting - A review of processing, microstructure and properties via the open data repository, FreezeCasting.net. *Prog. Matl. Sci.* **2018**, *94*, 243−305.

(124) Benad, A.; Jurries, F.; Vetter, B.; Klemmed, B.; Hubner, R.; Leyens, C.; Eychmuller, A. Mechanical Properties of Metal Oxide Aerogels. *Chem. Mater.* **2018**, *30*, 145−152.

(125) Zhang, H.; D'Angelo Nunes, P.; Wilhelm, M.; Rezwan, K. Hierarchically ordered micro/meso/macroporous polymer-derived ceramic monoliths fabricated by freeze-casting. *J. Euro. Ceram. Soc.* **2016**, *36*, 51−58.

(126) Kravanja, K. A.; Finsgar, M.; Knez, Z.; Knez Marevci, M. Supercritical Fluid Technologies for the Incorporation of Synthetic and Natural Active Compounds into Materials for Drug Formulation and Delivery. *Pharmaceutics* **2022**, *14*, 1670.

(127) Pravallika, K.; Chakraborty, S.; Singhal, R. S. Supercritical drying of food products: An insightful review. *J. Food Eng.* **2023**, *343*, 111375.